ATOMIZATION AND POWDER PROCESSING OF HIGH TEMPERATURE FERRITIC STAINLESS STEEL

Iver E. Anderson

222 Metals Development, Ames Lab. (USDOE), Iowa State Univ., Ames, IA 50011

E-mail: andersoni@ameslab.gov; Telephone: (515) 294-9791; Fax: (515) 294-8727

Joel E. Rieken

258-I Metals Development, Ames Lab. (USDOE), Iowa State Univ., Ames, IA 50011

E-mail: jrieken@iastate.edu; Telephone: (515) 294-9159; Fax: (515) 294-8727

David J. Byrd

109 Metals Development, Ames Lab. (USDOE), Iowa State Univ., Ames, IA 50011

E-mail: byrd@ameslab.gov; Telephone: (515) 294-5747; Fax: (515) 294-8727

ABSTRACT

Our studies strive to enable the implementation of several emerging Fossil Energy (FE) technologies that utilize metal powders of specific size ranges and types, which are either experimental or not produced efficiently by industry. In the current work, an innovative combination of high efficiency gas atomization with modified parameters and special powder alloy designs were employed to generate precursor powder for simplified processing of high temperature Fe-based alloys for FE applications. The widely practiced approach for producing oxide dispersion strengthened (ODS) ferritic stainless steels involved extensive mechanical alloying and thermal-mechanical processing and was so costly that previous commercial sources essentially ceased sales. In this new process (US Patents issued in April 2010 and June 2012), precursor ferritic stainless steel powders are oxidized *in situ* using a unique gas atomization reaction synthesis (GARS) technique. The as-atomized powders contain an ultra thin kinetically favored (*i.e.,* Cr-enriched) surface oxide. This surface layer is used as a vehicle to carry oxygen into the alloy microstructure after powder consolidation by hot isostatic pressing (HIP) to full density. Post-HIP heat treatments promote decomposition of the less stable prior particle boundary (PPB) oxide and enable oxygen diffusion and internal oxidation of the Y and other additions, e.g., Ti or Hf, within the matrix of each prior particle. The consolidation process and oxygen exchange reactions result in nano-metric Y-enriched oxide dispersoids distributed throughout the resulting microstructure. New studies included construction of analytical models of particle surface oxidation and droplet cooling as a function of particle size during the GARS process. These models will enable control of the oxygen addition which influences the desired ODS effects.

INTRODUCTION

A new molten metal processing technique involving rapid solidification has been implemented for the simplified production of precursor powder for oxide dispersion strengthened (ODS) ferritic stainless steel alloys [1-3]. These ODS alloys are ideal candidates for high temperature applications within future generation thermal power reactors (e.g., A-USC coal fired power plants)[4, 5]. This novel process is known as gas atomization reaction synthesis (GARS) [6]. During this process, a reactive atomization gas (i.e., Ar-O_2) is used to surface oxidize nascent ferritic stainless steel alloy droplets during primary break-up and rapid solidification of the atomized powders.

This rapid high temperature reaction is used to promote the formation of a metastable or kinetically favored (e.g., Cr-enriched) ultra thin (ξ < 150 nm) continuous surface oxide layer [2]. This oxide layer is used as a method to transport a specific amount of solid-state O into the consolidated microstructure. Elevated temperature heat treatment (during consolidation or post-consolidation) is then used to dissociate this Cr-enriched surface oxide phase, allowing O to diffuse away from prior particle boundaries (PPBs), which leads to the internal oxidation of more thermodynamically stable alloy additions (e.g., Y)[1]. It is important to note that the ability to completely dissociate all PPBs in the consolidated microstructure depends on control of the oxygen collected originally during GARS processing to ensure that it does not exceed the available concentration of stable oxide forming additions. This need for establishing "clean" PPBs is very important for achieving maximum strength levels for the resulting ODS microstructure [1, 2, 7].

This new processing technique contains many key advantages over mechanical alloying (MA), the conventional approach for producing precursor particulate for ODS ferritic stainless steel alloys [8-10]. These advantages can improve the production efficiency of precursor ODS ferritic stainless steel powders. GARS (atomization) processing has the potential of reaching commercial production rates up to 10-100 kg/min., which is orders of magnitude greater than the production rates associated with the traditional MA process [11, 12]. Gas atomization also could minimize batch-to-batch variability and strictly limit contamination within the powder particles. Furthermore, as-atomized precursor powder size selection offers the unique potential of controlling the final ODS microstructure as a function of solidification morphology, in which smaller powders with increased amounts of solute trapping resulted in finer and more uniformly distributed nano-metric oxide dispersoids [3].

The aim of this paper is to illustrate a droplet oxidation model, derived from theoretical powder particle cooling curves, as a method for controlling the *in situ* alloying addition of O during this GARS process.

EXPERIMENTAL

The composition for the as-atomized CR-alloy powders is shown in Table 1. The atomic percentage of each metallic constituent was identified using inductively coupled plasma / mass spectroscopy or atomic emission spectroscopy (ICP / MS or AES). Additionally, the chemistry of the surface oxide phase was evaluated using auger electron spectroscopy (AES) depth profiling and (in a few instances) transmission electron microscopy (TEM) with energy dispersive spectroscopy (EDS). The semi-quantitative assessment of the surface oxide phase revealed a primary enrichment of Cr and O with varying amounts of Fe, (Ti or Hf), or Y, depending on the CR-alloy chemistry (see Table 1).

Several of the key processing parameters include, atomization nozzle characteristics, pour tube geometry, and reactive gas composition (and injection point). These processing parameters can significantly influence the resulting O content in the atomized powders and the interlinked relationships between all processing parameters must be fully considered when establishing a predictive oxidation model for this GARS process. A more detailed discussion about the effect of each processing parameter can be found in the literature[13].

Table 1. Resulting as-atomized CR-alloy composition and resulting surface oxide phase.

Alloy	Fe (at.%)	Cr (at.%)	W (at.%)	Ti (at.%)	Hf (at.%)	Y (at.%)	Surface Oxide Phase
CR-112	83.24	15.52	-	-	-	0.09	Cr-enriched + Y and Fe*
CR-118	83.47	15.84	-	0.50	-	0.20	Cr-enriched + Ti and Fe*,#
CR-126	82.75	15.13	0.90	0.56	-	0.09	Cr-enriched + Ti*
CR-144	82.55	16.16	0.94	-	0.27	0.08	Cr-enriched + Fe*
CR-156	84.49	15.84	-	-	0.11	0.18	Cr-enriched*
CR-160	78.00	20.88	-	0.58	-	0.09	-
CR-164	83.59	15.55	-	-	0.12	0.09	Cr-enriched*,#
CR-166	83.53	15.91	-	0.12	-	0.09	Cr-enriched + Y and Fe*,#

* - Evaluated using AES depth profiles of the as-atomized powders

\# - Evaluated using TEM analysis with EDS line scans

RESULTS AND DISCUSSION

The oxidation kinetics of the predominant type of GARS reaction in the current series was empirically found to scale linearly with O_2 content in the reactive atomization gas. This finding is most well behaved for a set of Y-containing CR-alloy powders that used essentially identical GARS process parameters and resulted in a predominately Cr-enriched surface oxide layer (i.e., containing no appreciable Y – see Table 1), as displayed in Figure 1 (see dashed black linear

trend). For this reason, only CR-118, CR-126, CR-156, and CR-160 were used selectively to establish and compare a predictive oxidation model based on the theoretical cooling curves for a specific particle size range.

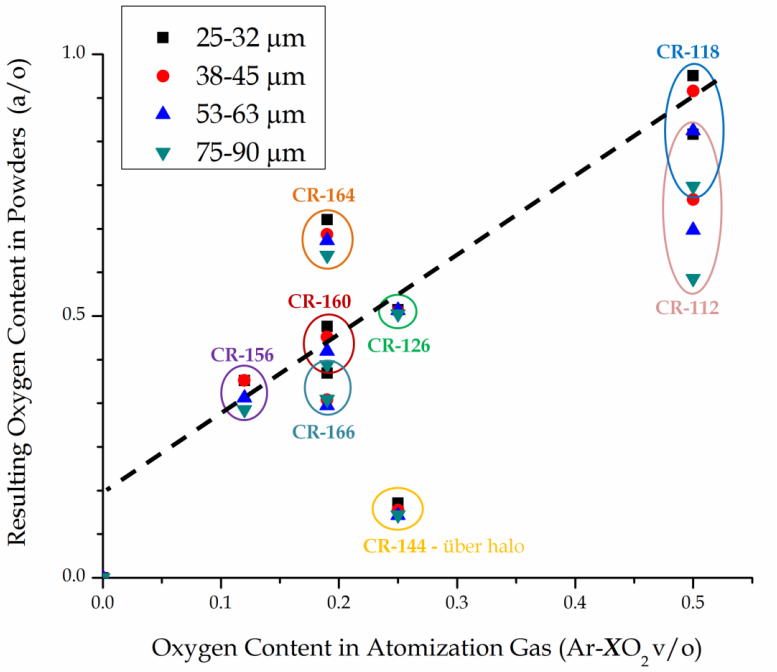

Figure 1. Resulting O content as a function of particle size and reactive atomization gas composition.

RESULTING OXIDE THICKNESS

The resulting surface oxide layer on select CR-164 powders was analyzed further using TEM with EDS. The TEM samples were prepared for analysis using focused ion beam (FIB) milling at the Electron Microscopy Center for Materials Research at Argonne National Laboratory–USDOE. More details about sample preparation can be found in the literature [14]. EDS linescans were used to qualitatively evaluate the chemistry of the surface oxide phase on these CR-164 powders. This analysis indicated that these CR-164 powders (dia. ~58µm) contained a Cr-enriched surface oxide layer (see Figure 2), which agreed quite well with a separate AES depth profile analysis (results not shown).

Interestingly, if the bulk O content associated with these powders was converted into a corresponding surface oxide layer thickness (assuming Cr_2O_3 phase formation, see Equation 1), the expected surface oxide layer thickness would be ~85 nm, which is near identical to the aforementioned (in Figure 2) TEM direct measurement for CR-164. For this reason, the bulk O content for each CR-alloy was converted into a surface oxide layer thickness (assuming Cr_2O_3 formation) and displayed in Figure 5a. It should be noted that this analysis is most likely only representative of those CR-alloys containing no appreciable Y in the Cr-enriched surface oxide phase, as displayed in Table 1.

$$\xi_{ox} = \frac{m_{O_2} W_{ox}}{S_p W_{O_2} \rho_{ox}} \qquad \textbf{Equation 1}$$

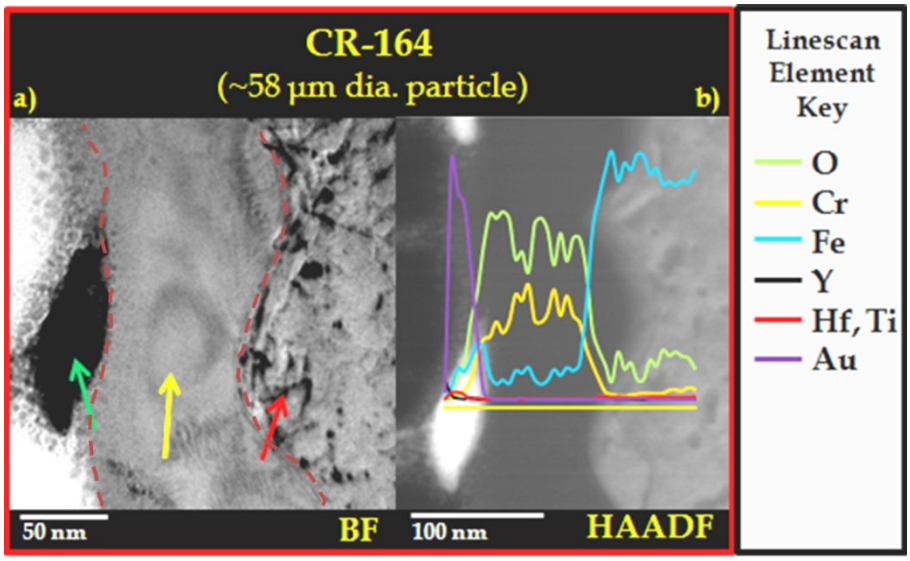

Figure 2. Companion images of, a) bright field (BF) TEM analysis with b) accompanying EDS linescan of the surface oxide phase (see yellow arrow, outlined by dashed red lines), indicating a Cr-enriched surface oxide phase.

THEORETICAL PARTICLE COOLING CURVES

Analysis of the high temperature oxidation kinetics associated with GARS processing was required to adequately predict O content (primarily as a surface oxide film) for the resulting precursor powders for the ODS alloys. For this reason, theoretical cooling curves for as-atomized ferritic stainless steel droplets were modeled, and oxidation profiles were extracted for specific powder size fractions. These oxidation profiles then were used to calculate a predicted surface oxide layer thickness.

The theoretical cooling curves were assembled using a similar method as previously demonstrated by Mathur et al. [15]. This model describes the thermal profile of as-atomized droplets as a function of droplet size (diameter), using droplet-gas interactions to describe particle acceleration and cooling rate. Thus, it provided a quantitative assessment of the oxidation time and temperature for a given particle size.

A description of the variables used for this model and specific thermodynamic and physical properties can be found in the literature[13]. The time resolution for this model was 1µs per time interval, except for during solidification when the time resolution was increased to 0.01µs.

PARTICLE VELOCITY

The mass flow rate of the atomization gas was calculated using the choked mass flow equation described by Poirier and Geiger, in combination with the calculated density of the atomization gas and an assumed discharge coefficient (see Equation 2-Equation 4) [16]. It should be noted that compressibility effects were not taken into consideration during this calculation (i.e., z = 1). Additionally, the atomization gas was assumed to be pure Ar, although it contained small additions of O_2.

$$\dot{m} = DA_j\sqrt{\gamma\rho_a P_a\left(\frac{2}{\gamma+1}\right)^{\frac{\gamma+1}{\gamma-1}}} \qquad \textbf{Equation 2}$$

Where, $\gamma = 1.67$ (specific heat ratio for Ar)

$$\rho_a = \frac{W_g P_a}{zRT_{g,a}} \qquad \textbf{Equation 3}$$

$$D = \left(\frac{1}{\beta_2} + e_f\right)^{-\frac{1}{2}}$$ **Equation 4**

Where, B_2=1(turbulent flow) and e_f=0.4 [16]

The initial velocity of the atomization gas was assumed to be at the speed of sound limit in Ar (i.e., M_a = 1) within each atomization gas jet passageway, since the critical pressure ratio (Equation 5) was satisfied for this GARS process [16].

$$if, \quad \frac{P_c}{P_a} \leq \left(\frac{2}{\gamma+1}\right)^{\frac{\gamma}{\gamma-1}} \quad then, \quad V_{g,a} = M_a c_{g,a}$$ **Equation 5**

Where, $M_a = 1$

Furthermore, the temperature and pressure of the gas within the atomization jets was calculated using Equation 6 and Equation 7 [16].

$$T_{g,j} = T_{g,a}\left(1 + \frac{\gamma-1}{2} M_a{}^2\right)^{-1}$$ **Equation 6**

Where, $T_{g,a}$= -40°C

(unpublished experimental results [17])

$$P_j = P_a\left(\frac{2}{\gamma+1}\right)^{\frac{\gamma}{\gamma-1}}$$ **Equation 7**

These values were then used to determine the velocity of the gas as it exited the jet holes, as described by the free expansion model (Equation 8-Equation 10), in which the gas accelerates to super-sonic velocity [16]. Moreover, the time required for the gas to achieve maximum velocity was neglected (i.e., acceleration was assumed to be instantaneous) and gas temperature was assumed not to change during expansion.

$$M_g = \sqrt{\left(\frac{2}{\gamma-1}\right)\left(\left(\frac{P_j}{P_c}\right)^{\frac{\gamma-1}{\gamma}} - 1\right)}$$ **Equation 8**

$$V_{g,i} = M_{g,j} c_{g,j}$$ **Equation 9**

$$c_{g,j} = \sqrt{\frac{\gamma R T_{g,j}}{W_g}}$$ **Equation 10**

The velocity profile of the atomization gas was assumed to follow the decay function described by Alam et al. (Equation 11), which was found to be dependent on the effective diameter (d_e) of the gas nozzle [18, 19].

$$V_g = V_{g,i}\left\{1 - \exp\left(-\frac{1}{2\eta\sqrt{\frac{\rho_c}{\rho_j}}\frac{x}{d_e} + \chi}\right)\right\}$$ **Equation 11**

Where, η=0.0841 and χ=0.06035 [18]

d_e=center bore of atomization nozzle [19]

The initial velocity of the as-atomized droplets was assumed to be zero, since initial droplet formation was observed to occur during shearing of the melt stream around the periphery at the base of the pour tube. This indicated that gas recirculation effects had fully interrupted the vertical descent of the molten stream, which forced the liquid to wet horizontally across the base of the pour tube prior to initial droplet formation. Additionally, it was assumed that the molten alloy instantaneously forms a predefined volumetric distribution of spherical droplets, thus neglecting the time required for droplet formation. This volumetric distribution was defined using experimental data from post-atomized size distribution analysis (results not shown).

Consequently, the velocity profile of the droplets is related to the velocity profile of the gas, as described by the momentum equation (Equation 12 and Equation 13), which is a function of the drag coefficient (Equation 14) as defined by the Reynolds number (Equation 15) [15, 20, 21].

$$\boldsymbol{F = m\left(\frac{dV_d}{dt}\right) = \left(\frac{C_D \rho_g V_r^2 A_d}{2}\right) + m_d g} \quad \textbf{Equation 12}$$

$$\boldsymbol{F = \left[\frac{3C_D \rho_g (V_g - V_d)\left|V_g - V_d\right| A_d}{4 d_d \rho_d}\right] + m_d g} \quad \textbf{Equation 13}$$

$$\boldsymbol{C_D = 0.28 + \left(\frac{6}{Re^{\frac{1}{2}}}\right) + \left(\frac{21}{Re}\right)} \quad \textbf{Equation 14}$$

$$\boldsymbol{Re_g = \frac{V_r d_d}{\nu_g}} \quad \textbf{Equation 15}$$

THERMAL PROFILE

Heat is extracted from the droplets through convective cooling between the droplets and atomization gas, and through radiation loss to the chamber wall for each given time interval (Equation 16). The heat transfer coefficient between the droplet and gas is inversely related to droplet size (d_d), i.e., Equation 17.

$$\boldsymbol{Q_d = \left(h_d S_d (T_d - T_g) + \sigma^* \epsilon S_d (T_d^4 - T_c^4)\right)} \quad \textbf{Equation 16}$$

$$\boldsymbol{h_d = \frac{k_g (2 + 0.6 Re^{\frac{1}{2}} Pr^{\frac{1}{3}})}{d_d}} \quad \textbf{Equation 17}$$

$$\boldsymbol{Pr_g = \frac{C_g \mu_g}{k_g}} \quad \textbf{Equation 18}$$

Where, C_g is constant for inert gases

The heat extracted from the particle is gained by the atomization gas, which in turn is cooled by the atomization chamber wall. This heat exchange sequence is thought to occur as a complete series during each time interval. The net heat increase in the atomization gas is shown in Equation 19 and Equation 20. It should be noted that the atomization chamber wall was assumed to maintain an average temperature of 70°C during the time-span of this model, a reasonable approximation for steady state of an industrial system that is actively cooled.

$$\boldsymbol{Q_g = \left[\sum_{d=5}^{82.5} \Phi_d \left(h_d S_d (T_d - T_g)\right)\right] - h_c\left(\pi d_c (x_{c,i} - x_{c,f})\right)\left(T_c - T_g\right)} \quad \textbf{Equation 19}$$

Where, $x_{c,i} - x_{c,f}$ is the total distance that the droplet travels during one time interval

$$\Phi_d = \frac{\dot{m}_m \Delta t \theta_d}{m_d}$$ **Equation 20**

Where, Φ = number of particles and θ_d = weight fraction of droplet distribution

The heat transfer coefficient between the atomization gas and atomization chamber wall is described using Equation 21-Equation 24 [22, 23].

$$h_c = \frac{Nu_g k_g}{d_c}$$ **Equation 21**

$$Nu_g = \frac{\left(\frac{f}{8}\right) Re_c Pr_g}{1.07 + 12.7\left(\frac{f}{8}\right)^{\frac{1}{2}}\left(Pr_g^{\frac{2}{3}} - 1\right)}$$ **Equation 22**

$$Re_c = \frac{V_g d_c}{\nu_g}$$ **Equation 23**

$$f = \left(\frac{1}{-1.8\, log\left[\frac{6.9}{Re_g} + \left(\frac{\varepsilon/d_c}{3.7}\right)^{1.11}\right]}\right)^2$$ **Equation 24**

Where, ε=0.002 [23]

Therefore, the net change in droplet temperature and atomization gas temperature for each given time interval was determined from Equation 25 and Equation 26, respectively.

$$\Delta T_d = \frac{Q_d \Delta t}{m_d C_d}$$ **Equation 25**

$$\Delta T_g = \frac{Q_g}{\dot{m}_g C_g}$$ **Equation 26**

COOLING CURVES

The resulting theoretical cooling curves with respect to droplet diameter as a function of time and temperature are displayed in Figure 3. The initial (sharp) inflection point on these curves (see red arrow in Figure 3) indicates the onset of solidification (i.e., start of recalescence) and the second inflection point (see green arrow in Figure 3) highlights the completion of solidification. Therefore, it can be seen that undercooling is inversely related to droplet size, i.e., smaller particles achieve greater undercooling prior to solidification.

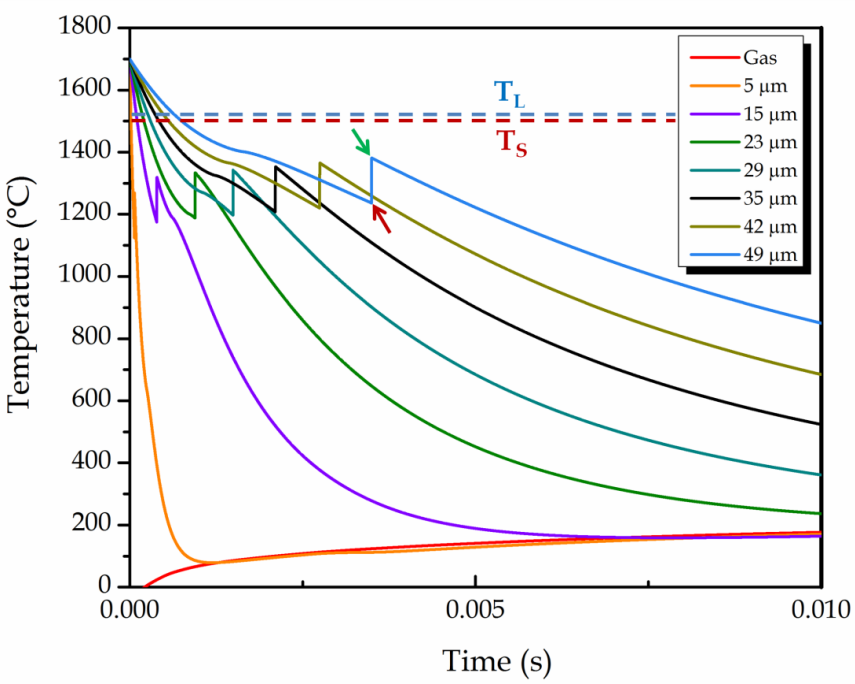

Figure 3. Theoretical particle cooling curves for CR-156 (T vs. t): note that the alloy solidus temperature (T_s) is marked by the horizontal dashed red line and liquidus temperature (T_L) is marked by the horizontal dashed blue line.

Furthermore, these curves illustrate the increased cooling rate associated with smaller droplets, as a direct consequence of the enhanced heat transfer coefficient due to the increased surface area to volume ratio of these powders. This implies that the larger droplets are subjected to prolonged oxidation at elevated temperature during this GARS process, which is consistent with experimental data of larger powders displaying a thicker surface oxide layer. It should be noted that particles with a dia. ≥ 49µm were omitted from these cooling curve figures, since the current state of this model did not accurately describe solidification when the temperature of these particles was raised above the solidus temperature (T_s) during recalescence.

GARS OXIDATION MODEL

The aforementioned theoretical droplet cooling curves were used to develop an oxidation model for this GARS process. It was assumed that the surface oxide layer will form as Cr oxide (i.e., Cr_2O_3) based on a compilation of experimental results (see Table 1). For this reason, the parabolic oxidation rate constant for Cr_2O_3, formulated from the results of Gulbransen et al. [24], was calculated for each time interval (i.e., 1µs) as the droplets were cooled (Equation 27). It should be noted that the parabolic oxidation pre-factor (B) was modified from 0.156 to 5.0, in order to achieve a better fit with the experimentally determined oxide layer thickness. Additionally, the parabolic rate constant was scaled with respect to the oxygen partial pressure (P_{O_2}) in the reactive atomization gas (see Equation 28). Notably, the parabolic rate constant was found to scale linearly with P_{O_2}(i.e., n=1), similar to the empirical relationship highlighted in Figure 1.

$$k_p = B exp\left(\frac{-E}{RT}\right) \quad \textbf{Equation 27}$$

Where, E=249 kJ/mol [24] and

B=5 $g^2cm^{-4}s^{-1}$ (this work)

$$k_p \propto \left(P_{O_2}\right)^{\frac{1}{n}} \quad \textbf{Equation 28}$$

Where, n=1

The change in mass associated with uptake of O during each time interval (i.e., 1μs) of oxidation was determined using Equation 29 [25]. The mass of O was then converted to oxide thickness using Equation 30 [25]. The net rate of oxidation then was evaluated using Equation 31. It should be noted that this oxidation reaction was deemed complete when the rate of oxidation decreased to a value less than 400 nm s^{-1}.

$$\Delta m_{O_2}(\Delta t) = \left(\frac{k_{p,i} + k_{p,f}}{2}\right)^{\frac{1}{2}} \cdot 2S_d\left(t_f^{\frac{1}{2}} - t_i^{\frac{1}{2}}\right) \quad \textbf{Equation 29}$$

$$\xi_{ox} = \frac{\Delta m_{O_2} W_{ox}}{S_d W_{O_2} y \rho_{ox}} \quad \textbf{Equation 30}$$

Where, $M_a O_y$

$$\delta = \frac{\Delta \xi_{ox}}{\Delta t} \quad \textbf{Equation 31}$$

The predicted surface oxide layer thickness as a function of reactive atomization time with respect to droplet diameter for CR-156 is shown in Figure 4. These calculations clearly indicate that surface oxide layer thickness increases with droplet diameter. Furthermore, each oxidation curve was found to contain a small inflection point (see red arrow in Figure 4), which represents solidification in the droplet. Interestingly, this model suggests that the majority of oxidation occurs prior to droplet solidification.

The predicted Cr_2O_3 surface oxide layer thickness was then compared to experimental data for CR-118, CR-126, CR-160, and CR-156 (i.e., the CR-alloys that contained a linear relationship identified in Figure 1, due to the formation of a similar Cr-enriched surface oxide phase under equivalent conditions) (see Figure 5 a). Remarkably, the predicted oxide layer thickness was found to agree quite well with the experimental oxide thickness data, especially for the CR-alloys atomized with a reaction gas containing a lower concentration of O_2. Therefore, this oxidation model is recommended as a processing tool to accurately predict the *in situ* alloying addition of O during future GARS trials.

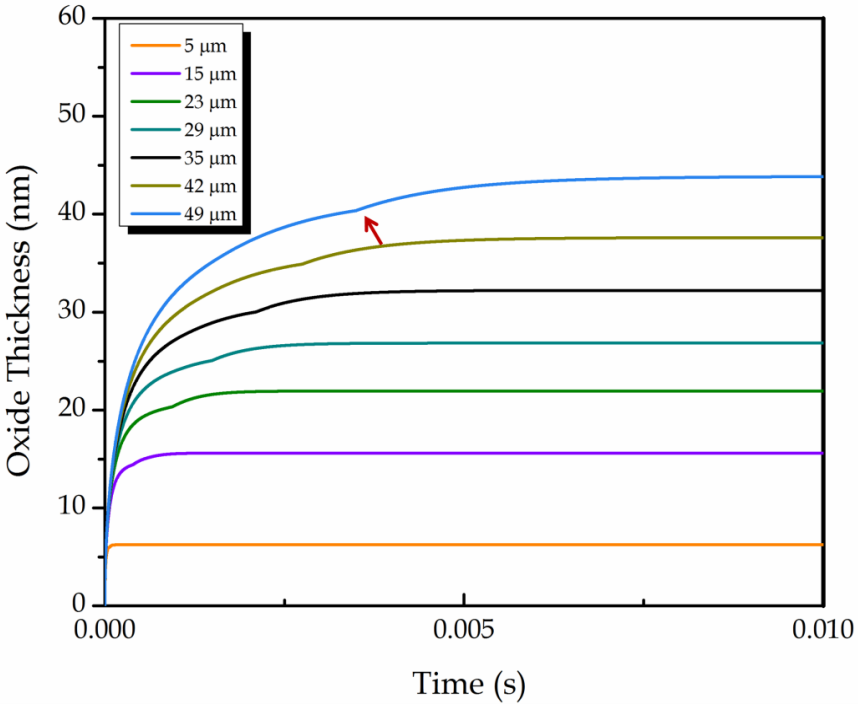

Figure 4. Predicted oxide layer thickness (CR-156) as a function of droplet diameters: note the red arrow highlighting the inflection point that indicates droplet solidification.

Analysis of the results of this oxidation model resulted in a range of parabolic rate constants (contained within the solid red lines in Figure 5 b), due to the aforementioned influence of P_{O_2}(i.e., different reaction gas compositions). The calculated parabolic rate constant as a function of temperature used for this oxidation model was compared to literature values for Cr_2O_3 oxidation on solid surfaces (see Figure 5 b). Interestingly, the results of this work coincide quite well with the central range of the literature values.

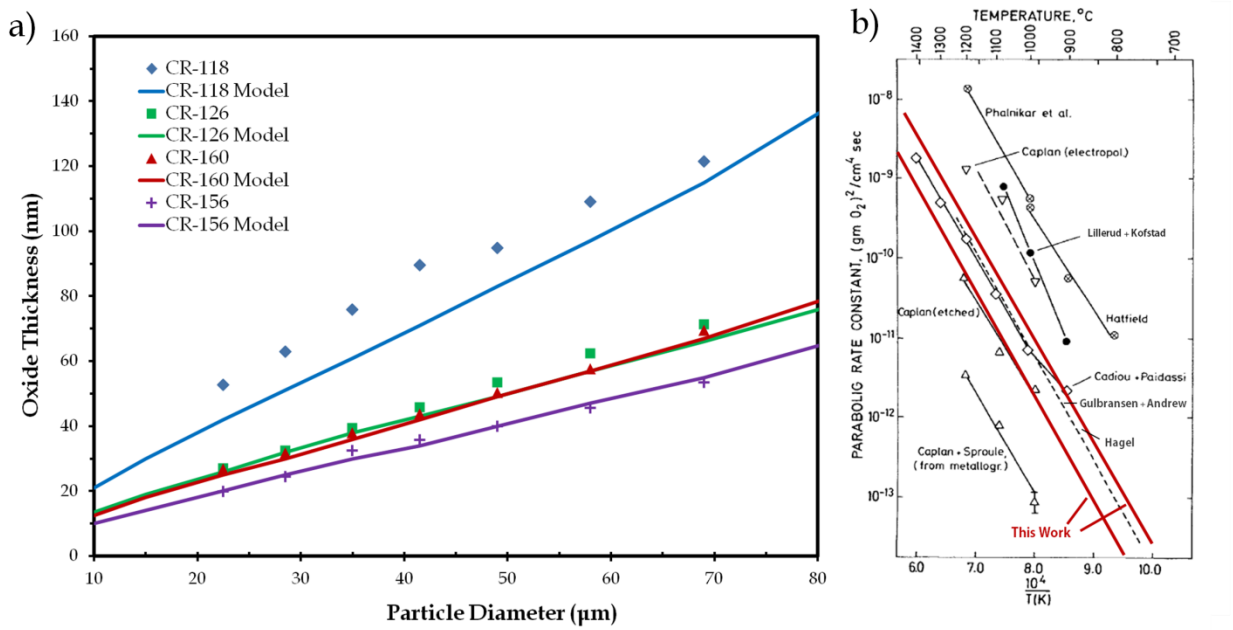

Figure 5. Comparison of a) predicted oxide layer thickness (solid lines) with experimentally determined (symbols) values (see Error! Reference source not found. **and b) the range of Cr_2O_3 parabolic rate constants (see red lines) used for the GARS oxidation model compared to literature values [24, 26-32].**

CONCLUSIONS

Gas atomization reaction synthesis (GARS) was used to produce precursor powders for ODS ferritic stainless steel alloys. This reactive gas atomization process resulted in the formation of an ultra thin (ξ < 150 nm) Cr-enriched metastable surface oxide layer on the powders. This surface oxide layer (upon decomposition) was utilized as an O reservoir for the formation of Y-enriched nano-metric dispersoids following consolidation and heat treatment of these precursor powders. A theoretical oxidation model, formulated from droplet cooling curves and based on the parabolic oxidation kinetics of Cr_2O_3, was designed as a method for predicting the resulting surface oxide layer thickness and corresponding O content as function of particle size. This oxidation model was shown to be a practical method to accurately predict the oxidation kinetics associated with GARS processing, assuming the formation of a Cr_2O_3 surface oxide phase. Furthermore, this oxidation model was suggested as a processing tool to predict and control O additions in future GARS trials.

ACKNOWLEDGEMENTS

Support from the Department of Energy, Office of Fossil Energy (ARM program) through Ames Laboratory contract no. DE-AC02-07CH11358 made this work possible. Additionally, the electron microscopy of the as-atomized surface oxide layer was accomplished at the Electron Microscopy Center for Materials Research at Argonne National Laboratory, a U.S. Department of Energy Office of Science Laboratory operated under Contract No. DE-AC02-06CH11357 by U. Chicago-Argonne, LLC. The authors also would like to thank A. Heidloff and M. Kramer from Ames Lab (USDOE) for their individual contributions to this paper.

REFERENCES

[1] I.E. Anderson, and R.L. Terpstra, "Dispersoid Reinforced Alloy Powder and Method of Making", U.S. Patent No. 7,699,905, 2010.

[2] J.R. Rieken, I.E. Anderson, M.J. Kramer, "Microstructure Evolution of Gas-Atomized Iron-Base ODS Alloys," *Int. J. Powder Metall.,* vol. 46, pp. 17-21, 2010.

[3] J.R. Rieken, I.E. Anderson, M.J. Kramer, G.R. Odette, E. Stergar, and E. Haney, "Reactive Gas Atomization Processing for Fe-based ODS Alloys," *J. Nucl. Mater.,* vol. 428, pp. 65-75, 2012.

[4] B.K. Kad, I. Wright, G. Smith, and R. Judkins, "Optimization of Oxide Dispersion Strengthened Alloy Tubes," in *19th Annual Conference on Fossil Energy Materials*, Knoxville, TN., 2005, pp. 1-9.

[5] J.P. Hurley, "Applications for Dispersion-Strengthened Alloys in Thermal Power Systems," in *21st Annual Conference on Fossil Energy Materials*, Knoxville, TN., 2007, pp. 29-37.

[6] I.E. Anderson, B.K. Lograsso, and T.W. Ellis, "Gas atomization synthesis of refractory or intermetallic compounds and supersaturated solid solutions", U.S. Patent No. 5,368,657, 1994.

[7] J.R. Rieken, I.E. Anderson, M.J. Kramer, Y.Q. Wu, J.W. Anderegg, A. Kracher and M.F. Besser, "Atomized Precursor Alloy Powder for Oxide Dispersion-Strengthened Ferritic Stainless Steel," in *Advances in Powder Metallurgy and Particulate Materials*, Princeton, NJ, 2008, pp. 324-342.

[8] J.S. Benjamin, "Mechanical Alloying - A Perspective," *Met. Powd. Rep.,* vol. 45, pp. 122-127, 1990.

[9] J.S. Benjamin, "Dispersion Strengthened Superalloys by Mechanical Alloying," *Metall. Trans.,* vol. 1, pp. 2943-2951, 1970.

[10] M.J. Alinger, G.R. Odette, and D.T. Hoelzer, "On the role of alloy composition and processing parameters in nanocluster formation and dispersion strengthening in nanostructured ferritic alloys," *Acta. Metall.,* vol. 57, pp. 392-406, 2009.

[11] R.M. German, *Powder Metallurgy & Particulate Materials Processing*. Princeton, NJ: Metal Powder Industries Federation, 2005.

[12] C. Suryanarayana, "Mechanical Alloying and Milling," *Prog. Mat. Sci.,* vol. 46, pp. 1-184, 2001.

[13] J.R. Rieken, "Gas atomized precursor alloy powder for oxide dispersion strengthened ferritic stainless steel", PhD Dissertation, in *Materials Science and Engineering,* Iowa State University, Ames, 2011, p. 335.

[14] J.R. Rieken, I.E. Anderson, M.J. Kramer, "Innovative Powder Processing of Oxide Dispersion Strengthened (ODS) Ferritic Stainless Steels," in *Advances in Powder Metallurgy and Particulate Materials*, San Francisco, CA, 2011, pp. 31-49.

[15] P. Mathur, D. Apelian, A. Lawley, "Analysis of the Spray Deposition Process," *Acta Metall. Mater.,* vol. 37, pp. 429-443, 1989.

[16] D.R. Poirier, G.G. Geiger, *Transport Phenomena in Materials Processing*. Warrendale, Pennsylvania: TMS, 1994.

[17] J.L. Meyer, 2011, *Iowa State University*, Ames, IA, private communication.

[18] M. Alam, J. Naser, G. A. Brooks, "CFD Simulation of Supersonic Oxygen Jet Behavior Inside a High Temperature Field," in *Seventh International Conference on CFD in the Minerals and Process Industries*, Australia, 2009, pp. 1-6.

[19] S.P. Mates, G.S. Settles, "A Study of Liquid Metal Atomization Using Close-Coupled Nozzles, Part 1: Gas Dynamic Behavior," *Atomization and Sprays,* vol. 15, pp. 19-40, 2005.

[20] A.A. Ranger, and J.A. Nicholls, "Aerodynamic Shattering of Liquid Drops," *A.l.A.A.J.,* vol. 7, pp. 285-290, 1969.

[21] R. Clift, J.R. Grace, and M.E. Weber, *Bubbles, Drops, and Particles*. New York: Academic Press, 1978.

[22] F.P. Incropera, D.P. DeWitt, *Fundamentals of Heat and Mass Transfer*, Fifth ed. New York: John Wiley & Sons, 2002.

[23] F.M. White, *Fluid Mechanics*, Seventh ed. New York: McGraw-Hill, 2011.

[24] E.A. Gulbransen, K.F. Andrew, "Kinetics of the Oxidation of Chromium," *J. Electrochem. Soc.,* vol. 104, pp. 334-338, 1957.

[25] O. Kubaschewski, B.E. Hopkins, *Oxidation of Metals and Alloys*, Second ed. New York: Academic Press Inc., 1962.

[26] P. Kofstad, K.P. Lillerud, "On High Temperature Oxidation of Chromium," *J. Electrochem. Soc.,* vol. 127, pp. 2410-2419, 1980.

[27] W.H. Hatfield, *J. Iron Steel Inst.,* vol. 115, p. 483, 1927.

[28] C.A. Phalnikar, E.B. Evans, and W.M. Baldwin, "High Temperature Scaling of Cobalt-Chromium Alloys," *J. Electrochem. Soc.,* vol. 103, pp. 429-438, 1956.

[29] W.C. Hagel, *Trans. Am. Soc. Met.,* vol. 56, p. 583, 1963.

[30] L. Cadiou, and J. Paidassi, *Mem. Sci. Rev. Metall.,* vol. 66, p. 217, 1969.

[31] D. Caplan, and G.I. Sproule, "Effect of Grain Structure on High-Temperature Oxidation of Cr," *Oxid. Met.,* vol. 9, p. 5, 1975.

[32] D. Caplan, and M. Cohen, *J. Electrochem. Soc.,* vol. 112, p. 5, 1964.